Analysis of Tevatron Flying Wire and Diffusion Measurement

August 28, 2009

Satomi Shiraishi

University of Chicago

Richard J. Tesarek

Fermi National Accelerator Laboratory

Abstract

Particle diffusion out of the beam core causes beam loss and contributes to a shorter liftetime of a circulating beam, higher radiation doses to accelerator components, and backgrounds in experiments which use the beam. We present an analysis of measurements of the proton diffusion rate using the Tevatron Flying Wires located at E11. In the Flying Wire data, we identify systematic effects such as detector dependence on beam intensity, different angular acceptance for upstream and downstream profiles, and asymmetric beam profiles. We calibrate those effects and propose a method to interpret asymmetric beam profiles. Using this new technique, we study proton beam diffusion rate during HEP collision in 10 typical stores. We measure $(8.93 \pm 0.01) \times 10^{-3}$ mm^2/hour and $(6.24 \pm 0.01) \times 10^{-3}$ mm^2/hour of horizontal and vertical diffusion rate, respectively.

1 Introduction

It is critical for the operation of a particle accelerator or storage ring to have a good understanding and control of the particle trajectories. Noise in RF and power supplies, beam-gas interactions, and intra-beam scattering increase the oscillation amplitude of the beam particles [1]. This process leads to a slow growth in the beam width and is referred to as transverse beam diffusion. Measuring this beam growth rate allows one to infer the transverse emittance growth for the stored beam. We use a Flying Wire (FW) beam profile monitor to measure beam width as a function of time [2]. We analyze FW data from the E11 horizontal and vertical systems using the low-gain

Table 1: List of stores analyzed. All stores are selected from June 2008.

Store	Date	Store Lengh [hr.]	Initial Lumi. [E30/cm^2/s]	No. of p [E9]	No. of $\bar{p}$ [E9]
6200	06.06	25.0	295.3	9755	2739
6203	06.07	13.5	287.0	8968	3040
6214	06.10	24.5	211.4	9905	2314
6215	06.11	28.5	214.6	9989	1948
6216	06.12	18.2	191.2	9798	2140
6239	06.21	16.0	271.7	9419	2892
6240	06.21	28.7	278.7	9525	2859
6245	06.24	17.9	201.4	9512	1939
6250	06.26	17.3	281.7	9346	2813
6251	06.27	20.4	267.7	9256	2707

scintillator paddle. After studying features of the data, we calibrate the data against the Fast Bunch Integrator (FBI) and remove some systematic effects [3]. Then, we measure beam width growth rate for 10 typical stores with FW data taken during High Energy Physics (HEP) in June 2008. The date, length, initial luminosity, and particle intensities for those stores are listed in Table 1.

2 Flying Wire Apparatus

The FW is a beam profile monitor located in the E11 and E17 sections of the Tevatron. Details of the FW system are described elsewhere [4]. The E11 section of the Tevatron is a low dispersion region. In E11, horizontal and vertical FW cans are installed along with a common low gain and high gain scintillation paddles that detect scattering from the both wires. We use only the low gain paddle data for the analysis described in this note. A schematic of a FW system is shown in Figure 2. Each FW can contains monofilament carbon fiber of thickness 5 μm which is placed in a fork at a radius of 96.5 mm from the drive motor axis. The wire is passed through the beam at 6.6 m/s and interacts with the beam twice. These interactions, which we call upstream and downstream interactions, are roughly 18 cm apart [2, 5].

Some of the scattered and secondary particles are detected by a scintillation counter located downstream. The current measured by the counter is therefore related to the beam profile. The current is integrated over 36 separate time windows corresponding to the 36 bunches for each encoder position. The wire can move in a clockwise (CW) or counter clockwise (CCW) direction in each plane. The encoder counts are recorded as a function of time to give one wire position information. The ADC counts along with position information from the encoder counts construct beam profiles. A total of 72 profiles, two profiles for each of the 36 bunches, are recorded for each view (horizontal/vertical) in a fly. A FW measurement is taken every hour during a Tevatron

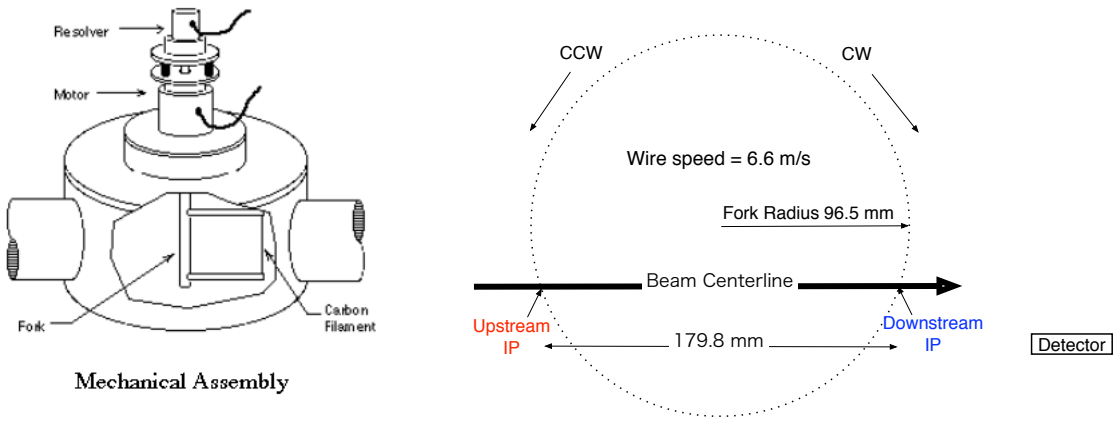

Figure 1: Schematics of FW systems. Left: mecahnical assembly of FW cans taken from [4]. Right: The FW viewed from the top. Dots on the circle represent the path of the wire. Each dot is a location of wire at a given time. The wire is vertical into the paper.

store.

The recorded encorder and ADC counts are first processed using a LabVIEW program, "FW Offline Analysis," maintained by J. Zagel and D. Slimmer [6]. This program converts the ADC counts to voltage and encoder counts to projected position on the plane perpendicular to the beam. Conversion from ADC to volts is performed using,

$$V(x) = k * (ADC - b), \tag{1}$$

where V is the beam loss measured in volts, $b = 2048$ is the baseline, and $k = -0.002441$ volts/count is the conversion factor.

The coordinate system used to convert encoder counts is shown in Figure 2. Encoder counts, θ_E, are converted to position on the projected plane using,

$$X = X_0 + r \cdot \sin(\theta_0 + \mathrm{K_E}\theta_\mathrm{E} + \theta_\mathrm{R}), \tag{2}$$

where $X_0 = -36.5$ mm, $r = 96.5$ mm, $\theta_0 = -1.57$, and $\mathrm{K_E} = -0.3834$. The parameter, θ_R, is an angular offset calculated in the analysis program to constrain the upstream and downstream peaks to the same position. The calculation of θ_R is termed autorotation and its effect is studied in Section 3.5. In addition, the data is truncated to 100 points around the peak of the beam profiles and saved as a LabVIEW file. After this preprocessing, we obtain beam profiles with a window size of roughly ±6mm around the peak. We use this preprocessed data for our beam width analysis since raw data is unavailable. ASCII format beam profiles are extracted from the LabVIEW files using `FW ExtractRawData.vi` written by D. Slimmer for this analysis. Figure 3 shows typical profiles from the flying wire system processed as described above.

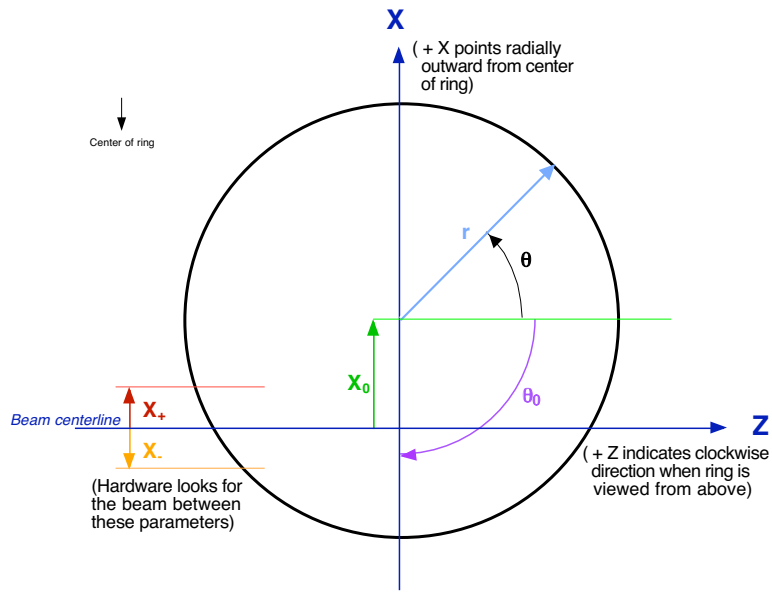

Figure 2: Flying Wire horizontal coordinate system taken from [5].

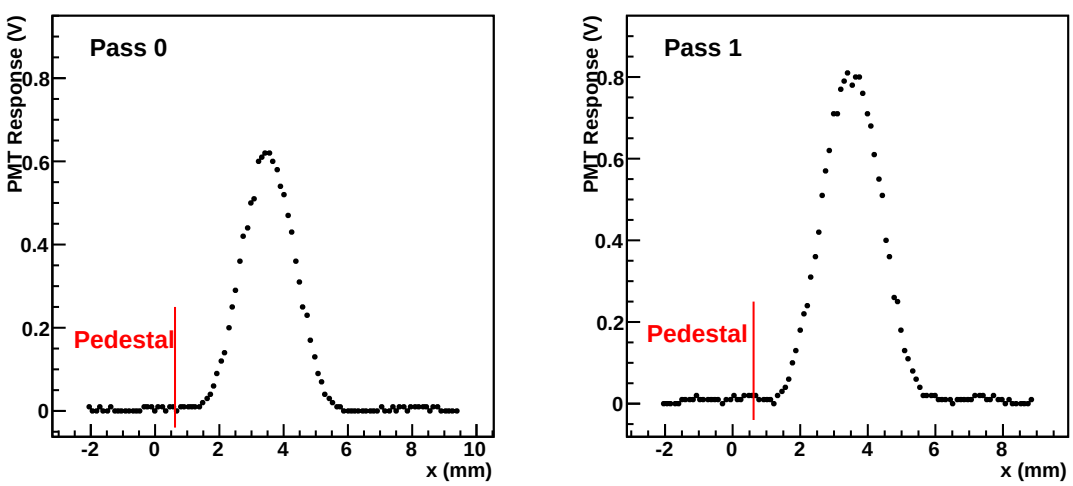

Figure 3: Typical beam profiles from the E11 vertical flying wire for two the two passes through the beam. Arrows indicate the first 25 points used in calculating pedestals. Profiles from E11 horizontal and E17 are similar.

3 Calibrations

In order to extract meaningful information from the FW data, one needs to convert the measured voltages as a function of wire position (x) to a number of protons per unit length ($d\Lambda(x)/dx$). This conversion is given by

$$\rho(x) = \frac{A}{C_z(I_{beam})} \left(V(x) - V_0\right), \tag{3}$$

where V_0 is the baseline offset, A is a conversion from measured voltage to particles per unit length and $C_z(I_{beam})$ corrects for the relative angular detector acceptance for the upstream/downstream wire positions and beam intensity dependent (I_{beam}) effects in the detector response. The following sections describe how we arrive at the values and functional forms of the corrections in detail. *Each store is calibrated independently.*

3.1 Pedestal

The calibration begins by determining the value of the average offset voltage (pedestal) from the data. The first 25 points in a profile are used to calculate an average pedestal and RMS (σ_{ped}) for that pedestal. These data points correspond to the very edge of a profile when the wire is far (≈ 5 mm) from the beam. Figure 4 shows the pedestal mean and RMS for each bunch in a single fly taken in store 6240. Figure 5 shows the pedestal mean and RMS for bunch 1 as a function of time into the store. The data indicate that the mean and RMS of a pedestal remain constant as a function of time. We calculate a pedestal for each profile.

3.2 Measurement Uncertainties

In our analysis, we assign an uncertainty, $\sigma(x)$, on each data point to evaluate uncertainty of the fit and consequently of the measurements. We estimate the uncertainty for each measurement as

$$\sigma(x) = \sqrt{\sigma_{ped}^2 + \alpha y'(x)^2}, \tag{4}$$

where the first term represents electronic noise and the second term represents uncertainty from counting particles with the counter. We define σ_{ped} as the RMS of 25 data points when the wire is out of beam. Measured amplitude is $y'(x)$. The constant α is defined so that the pull distribution is centered around zero and has a unit width, where the pull is defined as

$$\text{pull}(x) = \frac{A_{data}(x) - A_{fit}(x)}{\sigma(x)}. \tag{5}$$

The fitted value, $A_{fit}(x)$, is determined from fits of a double Gaussian probability density function (PDF) to beam profiles. The constant α is determined using fly 1213343860 in store 6216 and listed in Table 2. The pull as a function of horizontal position and pull distributions are shown in Figure 6 and indicate that the estimate on uncertainty is reasonable. The same α is used for all 10 stores.

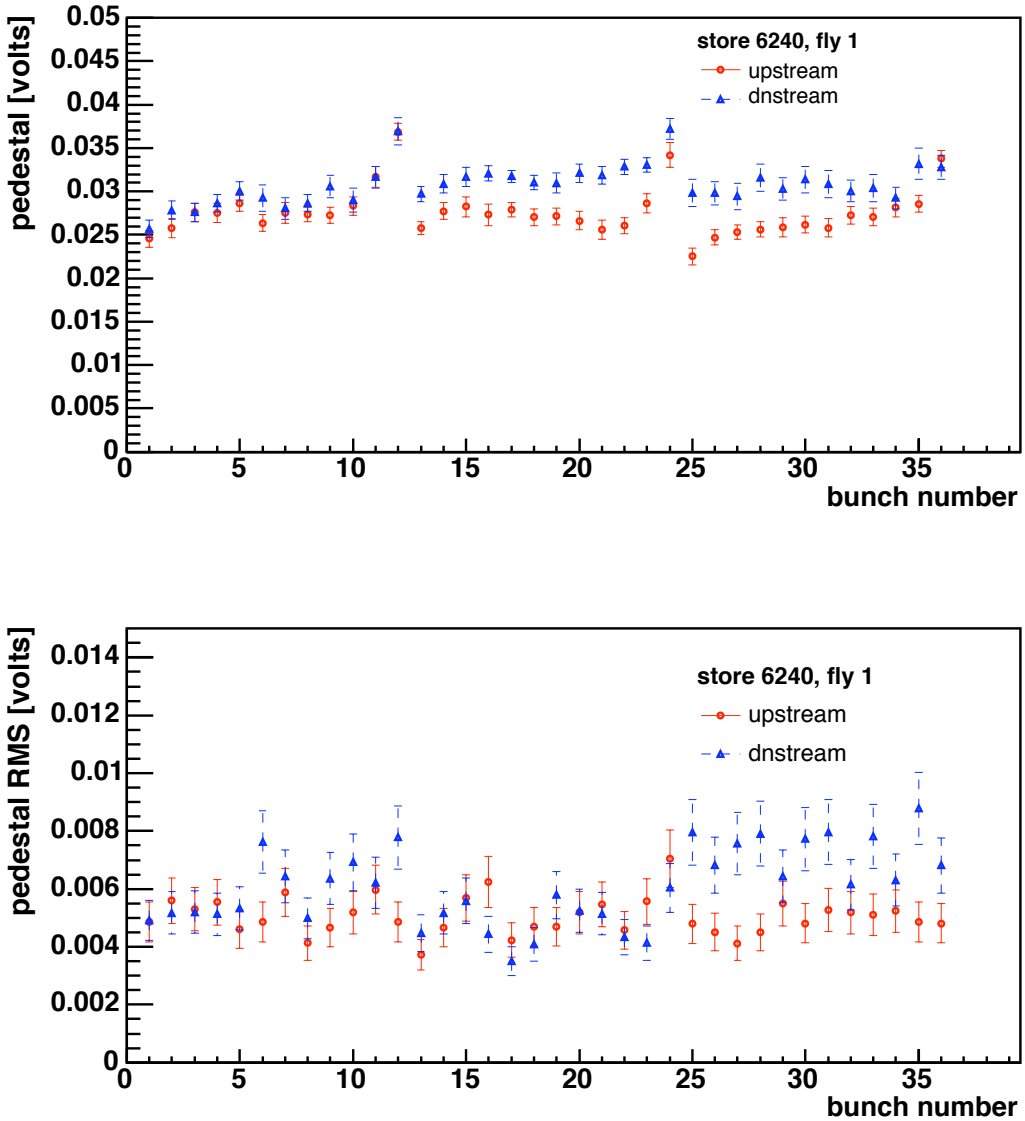

Figure 4: Pedestal mean (top) and RMS(bottom) for all 36 bunches from one horizontal fly taken in store 6240.

Table 2: The constant α for uncertainty calculation.

	Upstream	Downstream
	pass0 for H pass1 for V	pass1 for H pass0 for V
Horizontal	0.235	0.355
Vertical	0.244	0.194

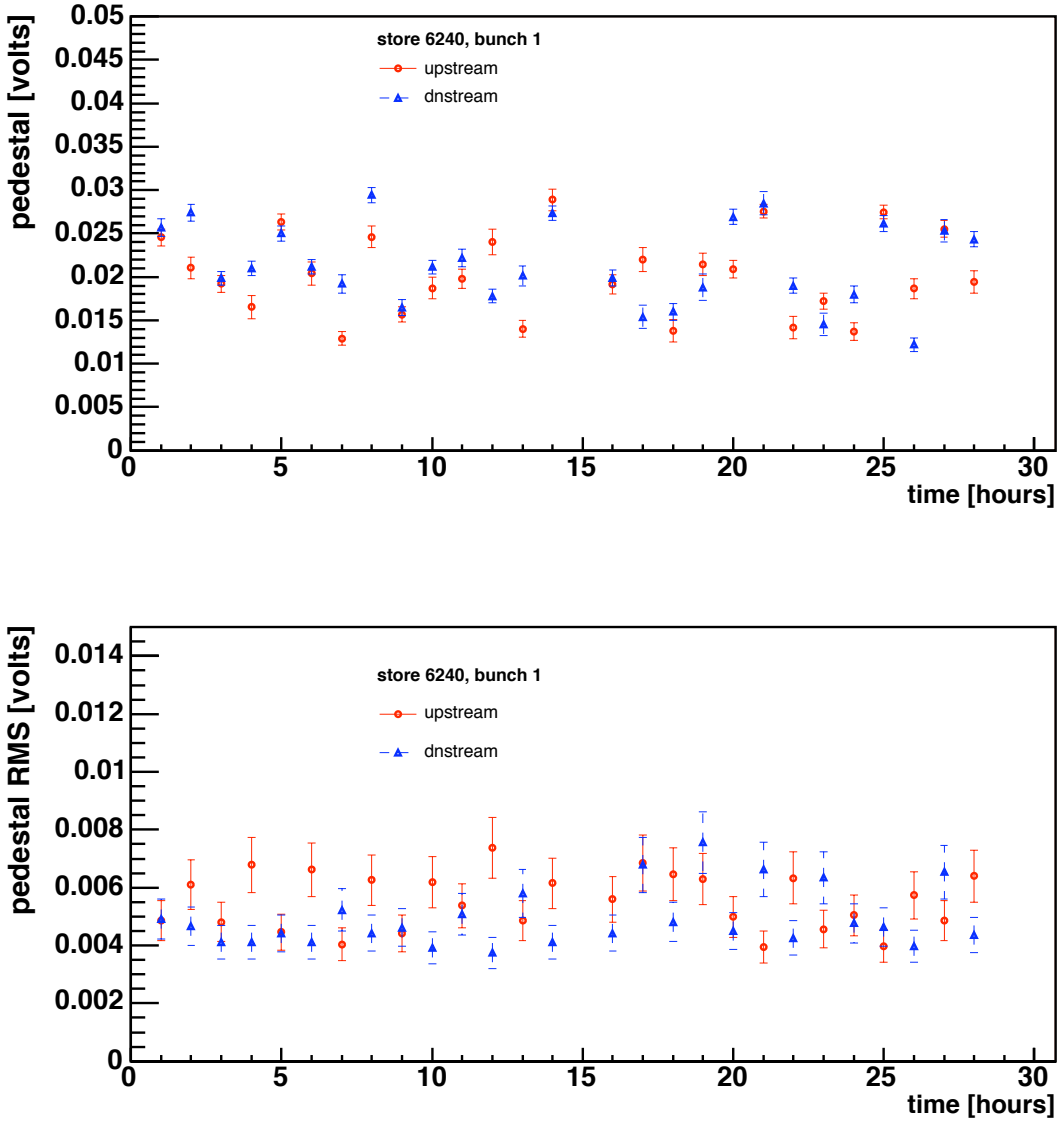

Figure 5: Pedestal mean (top) and RMS (bottom) as a function of time for bunch 1 in store 6240 (horizontal wire). Flys are taken every hour.

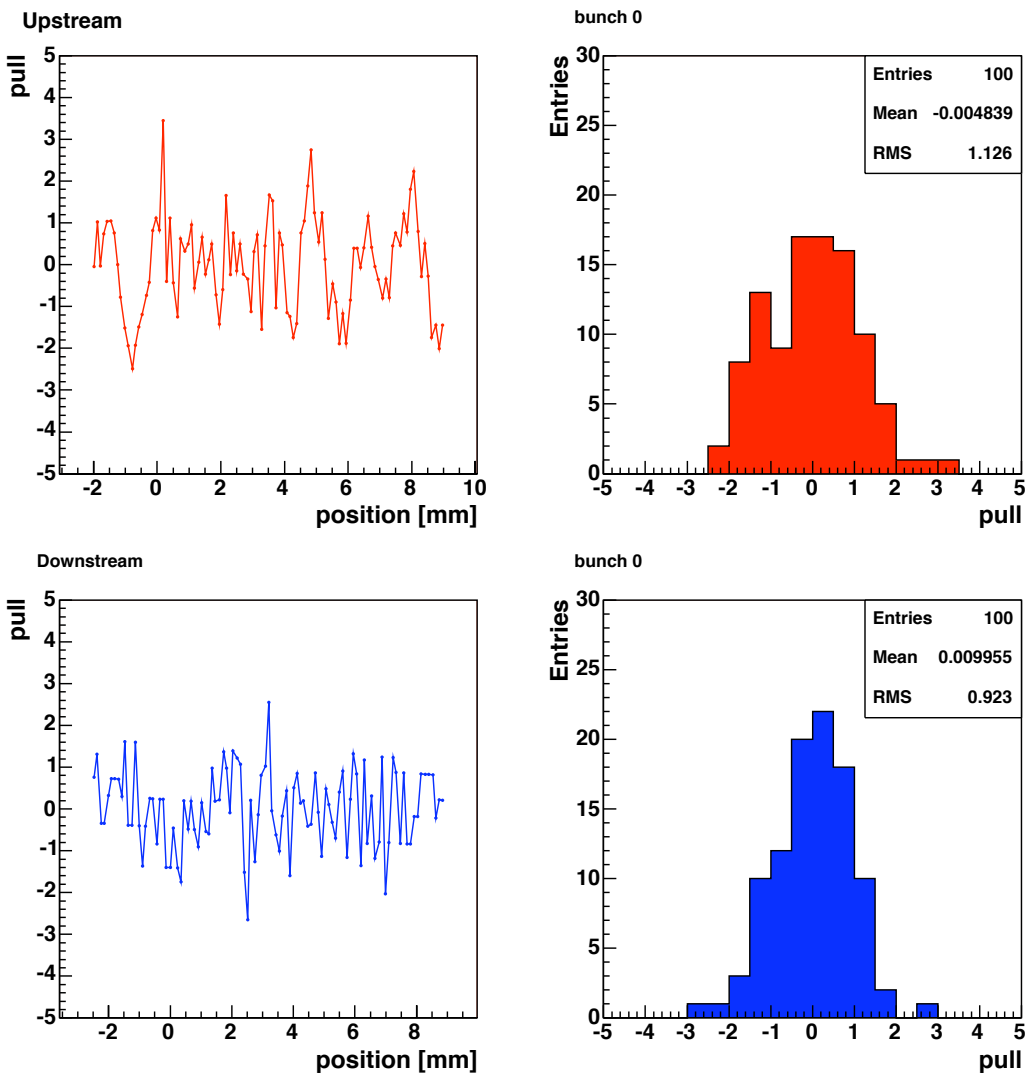

Figure 6: Pull as a function of position (left) and pull distribution (right) for the first bunch in store 6216 fly 1213333060. Upstream is red(top) and downstream is blue(bottom).

3.3 Conversion to Particle Density

The processed data is converted to particle density, $\rho_0(x)$, using

$$\rho_0(x) = A * (V(x) - V_0), \tag{6}$$

where $V(x)$ is the FW measurement in volts, V_0 is pedestal calculated as described in Section 3.1, and A is the scaling constant that converts volts to particle density. The scaling constant, A, is the average number of particles measured ($\langle I_{beam} \rangle$) by the Fast Bunch Integrator (FBI) divided by the average area under upstream FW beam profiles,

$$A = \frac{\langle I_{beam} \rangle}{\langle \int_{profile} (V(x) - V_0) dx \rangle}. \tag{7}$$

Both averages are taken over the 36 bunches. Store 6184 fly 1212320978 (6/1/08 6:49:38AM) is randomly chosen to calculate A. Figure 7 shows the proton intensity from the FBI (C:FBIPNG) measurements from a typical store (store 6216) for bunches 1–4. The Figure indicates that each bunch decreases in intensity during a store. Separate conversion factors, A_H and A_V, are calculated for the horizontal and vertical measurements, respectively. These conversion factors are listed in Table 3. The same value of the conversion factors are used for both upstream and downstream profiles and for all 10 stores. The next section describes the correction to account for differences between upstream and downstream profiles.

Table 3: Scaling constant used to convert beam profiles to particle density profiles.

	FBI [E09]	FW area [Volts-mm]	A [E09/volts-mm]
Horizontal	223.09 ± 7.89	1.71 ± 0.06	130.46
Vertical	223.09 ± 7.89	1.63 ± 0.01	136.87

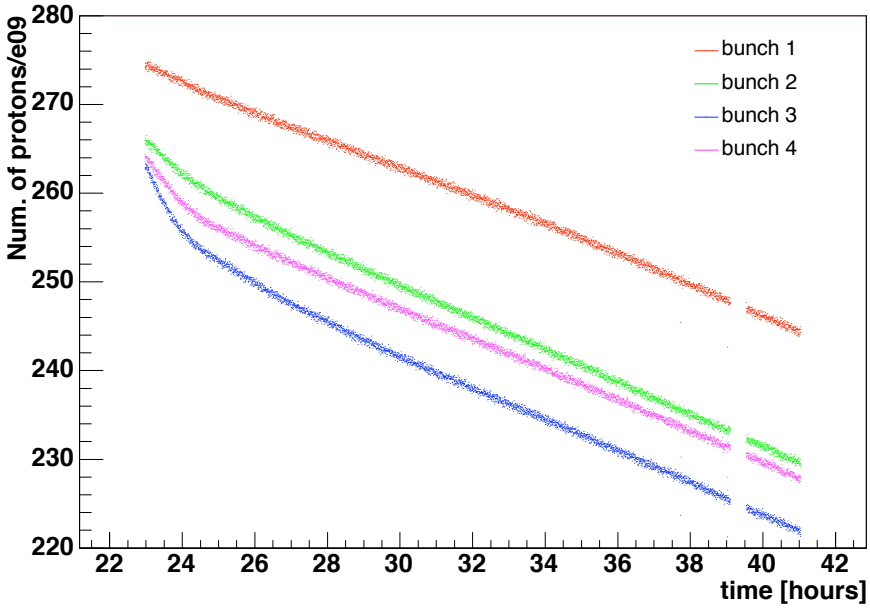

Figure 7: Fast Bunch Integrator data from store 6216, for bunches 1–4. The remaining 32 bunches exhibit similar behavior.

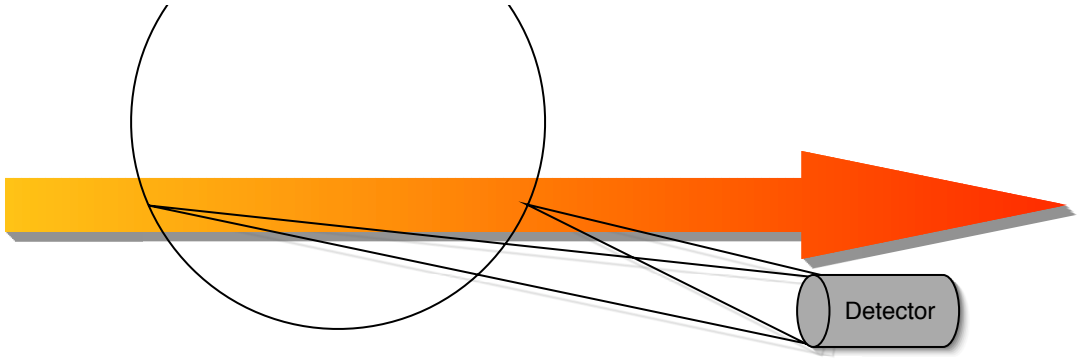

Figure 8: Schematic showing the locations of the upstream and downstream portions of a fly compared with the detector. Note that the detector subtends a smaller solid angle for the upstream portion of the fly than the downstream portion.

3.4 Angular Acceptance Beam Intensity Effects

3.4.1 Detector Acceptance

A single scintillation paddle is located downstream of the E11 horizontal and vertical FW cans. The paddle is located closer to the downstream interaction point (IP) of each can (Figure 8). As viewed from each IP, the counter subtends smaller solid angle for the upstream IP than the downstream IP. Naively, the downstream profiles that subtends the larger solid angle should have larger area profile than upstream profiles. The FW Offline Analysis program names the two profiles as pass0 and pass1 for each bunch. Since pass1 constantly has a larger area under the profile than pass0 for horizontal profiles, we label horizontal pass0 as upstream profiles and pass1 as downstream profiles. On the other hand, pass0 has larger area under profiles than pass1 for vertical profiles. Therefore, we label pass0 is downstream and pass1 is upstream profile for vertical profiles. Although our naming of two profiles as upstream and downstream profiles help give intuitive understanding, our analysis does not depend on the naming convention.

The effect described above is illustrated in Figure 9 which shows the pedestal subtracted detector response from a single fly recorded during store 6216. The pedestal subtracted detector response, R is given by

$$R = \int_{profile} (V(x) - V_0)\, dx. \tag{8}$$

Both upstream and downstream portions of the fly are shown for the horizontal and vertical profiles. Note that the downstream profiles are, on average, $\sim 11\%$ and $\sim 20\%$ greater than upstream for horizontal and vertical profiles, respectively. Moreover, the average area under the profiles measured by the horizontal system is $\sim 25\%$ greater than that measured by the vertical system.

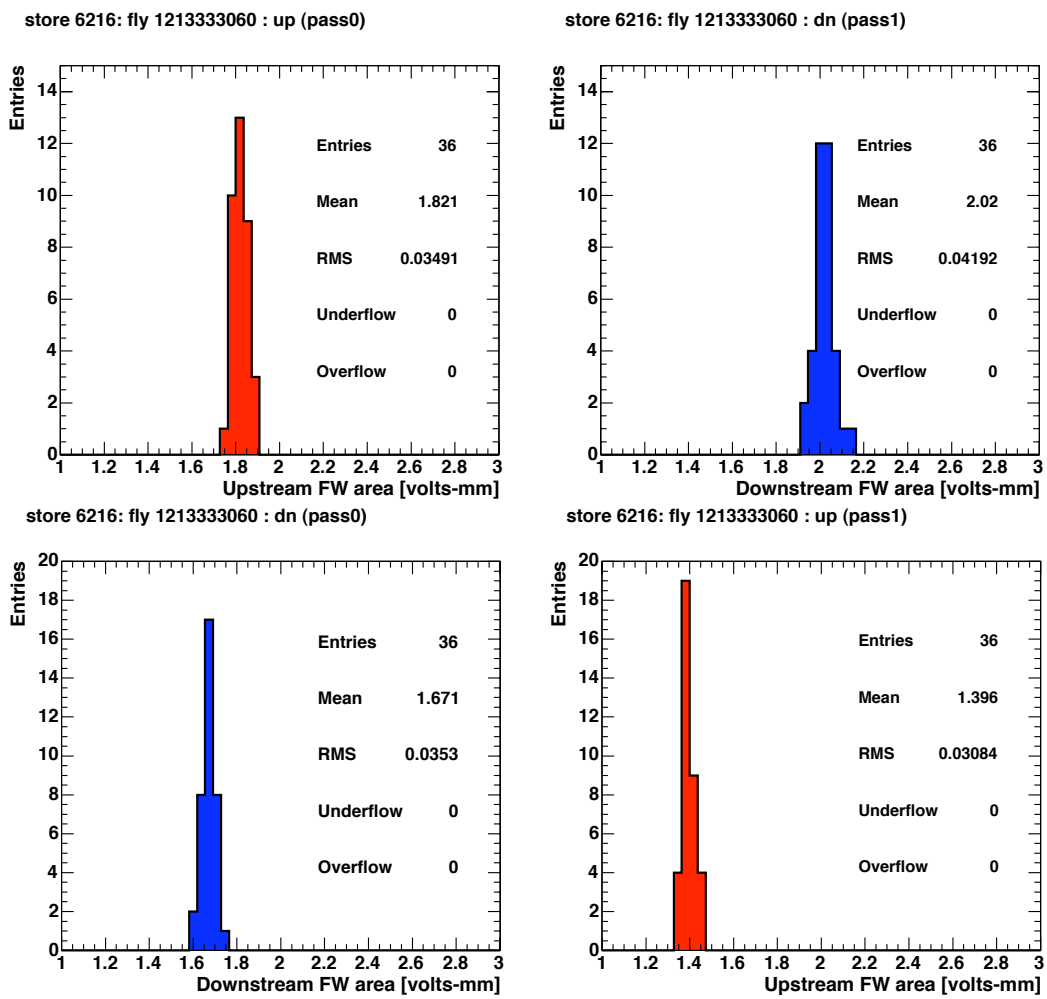

Figure 9: Bunch intensity measured by the horizontal (top) and vertical (bottom) FW for fly 1213333060 in store 6216. Pass0 is on the left and pass1 is on the right.

3.4.2 Beam Intensity Dependent Detector Response

The FW detector response depends on beam intensity. After we calibrate the area under the beam profile to be equal to FBI as described in Section 3.3, we expect the ratio of FW area to FBI intensity to be 1. However, a plot of the ratio of FW area over FBI intensity as a function of FBI intensity has a significant slope as shown in Figure 10. This suggests that the sensitivity of the FW detector depends on beam intensity as seen by the PMT assuming FBI measurements are accurate. The offset between upstream and downstream graphs indicates the difference in angular acceptance as discussed above.

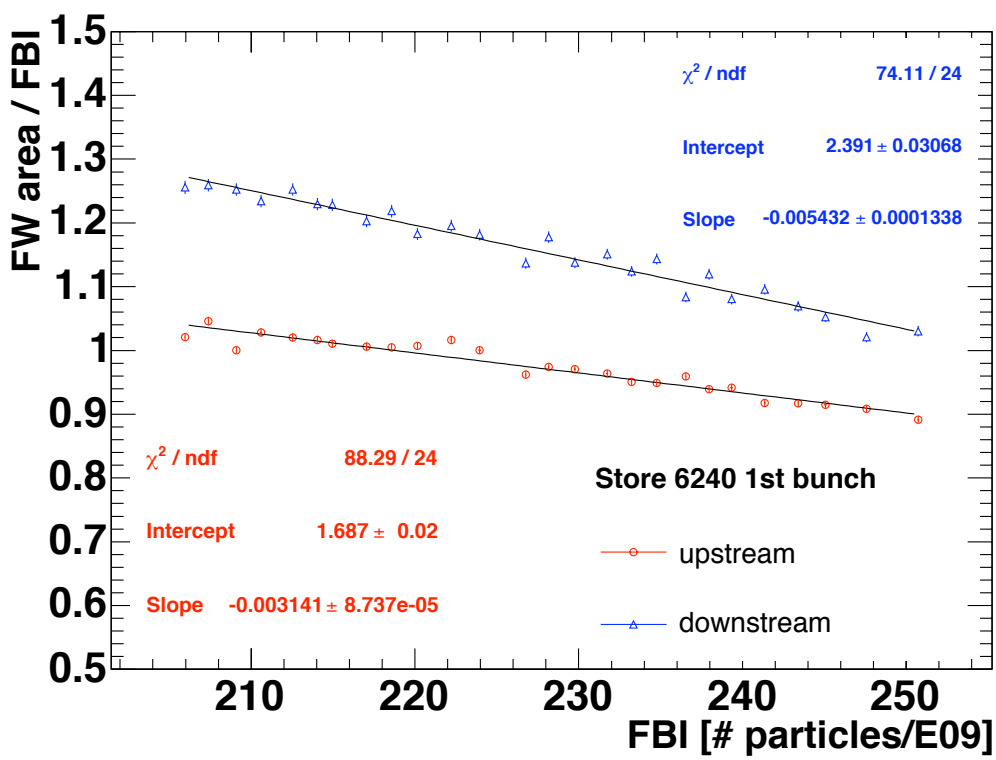

Figure 10: Horizontal FW area normalized by FBI as a function of FBI. The graph is for the first bunch in store 6240.

3.4.3 Acceptance and Intensity Calibration

The differences in the particle acceptance angle between the upstream and downstream profiles (Section 3.4.1), and the detector response dependence on beam intensity (Section 3.4.2) are calibrated simultaneously. In order to correct for the intensity dependence, we define a linear correction function using the following formula:

$$C_z(I_{beam}) = s * I_{beam} + r_0, , \tag{9}$$

where $C_z(I_{beam})$ is the correction factor, I_{beam} is the intensity measured by the FBI, and s and r_0 are the slope and intercept taken from a fit of the rato FW/FBI as a function of I_{beam} (FBI) as shown in Figure 10. Measurements for the first bunch are used to define the correction function for all bunches. The correction function is defined individually for upstream and downstream for each store to calibrate against the difference in the angular acceptance. The calibration is applied to all bunches by dividing the measured particle density, ρ_0, by the correction factor $C_z(I_{beam})$:

$$\rho(x) = \rho_0(x)/C_z(I_{beam})., \tag{10}$$

where $\rho_0(x)$ is defined in equation 6. Table 4 and 5 list the slopes and intercepts for the horizontal and vertical correction functions for the 10 stores. The values of the horizontal and vertical slopes and intercepts are shown as a function of store in Figure 11.

Table 4: Slope and intercept of the horizontal correction function (equation 10) for the 10 stores.

	Upstream (pass0)		Downstream (pass1)	
Store	s	r_0	s	r_0
6200	-0.003627 ± 0.000093	1.879 ± 0.022	-0.006161 ± 0.000145	2.673 ± 0.034
6203	-0.002587 ± 0.000170	1.587 ± 0.038	-0.005108 ± 0.000256	2.334 ± 0.057
6214	-0.003048 ± 0.000090	1.661 ± 0.021	-0.004558 ± 0.000136	2.163 ± 0.031
6215	-0.003247 ± 0.000082	1.756 ± 0.020	-0.005083 ± 0.000125	2.356 ± 0.030
6216	-0.003362 ± 0.000150	1.824 ± 0.039	-0.006170 ± 0.000224	2.704 ± 0.058
6239	-0.003693 ± 0.000223	1.796 ± 0.052	-0.006071 ± 0.000338	2.506 ± 0.078
6240	-0.003141 ± 0.000087	1.687 ± 0.020	-0.005432 ± 0.000134	2.391 ± 0.031
6245	-0.005181 ± 0.000270	2.203 ± 0.066	-0.008200 ± 0.000404	3.099 ± 0.098
6250	-0.003171 ± 0.000157	1.691 ± 0.037	-0.005782 ± 0.000237	2.471 ± 0.056
6251	-0.002842 ± 0.000114	1.587 ± 0.025	-0.005376 ± 0.000174	2.325 ± 0.039

Figure 12 (top) shows the ratio of FBI and FW intensity as a function of FBI after the calibration. The ratio is 1 and slope is 0 by construction for the first bunch. The bottom figure shows that the calibration is reasonable for other bunches.

In order to check that the calibration is working properly, beam intensity measured by FW is plotted as a function of time before and after the calibration in Figure 13.

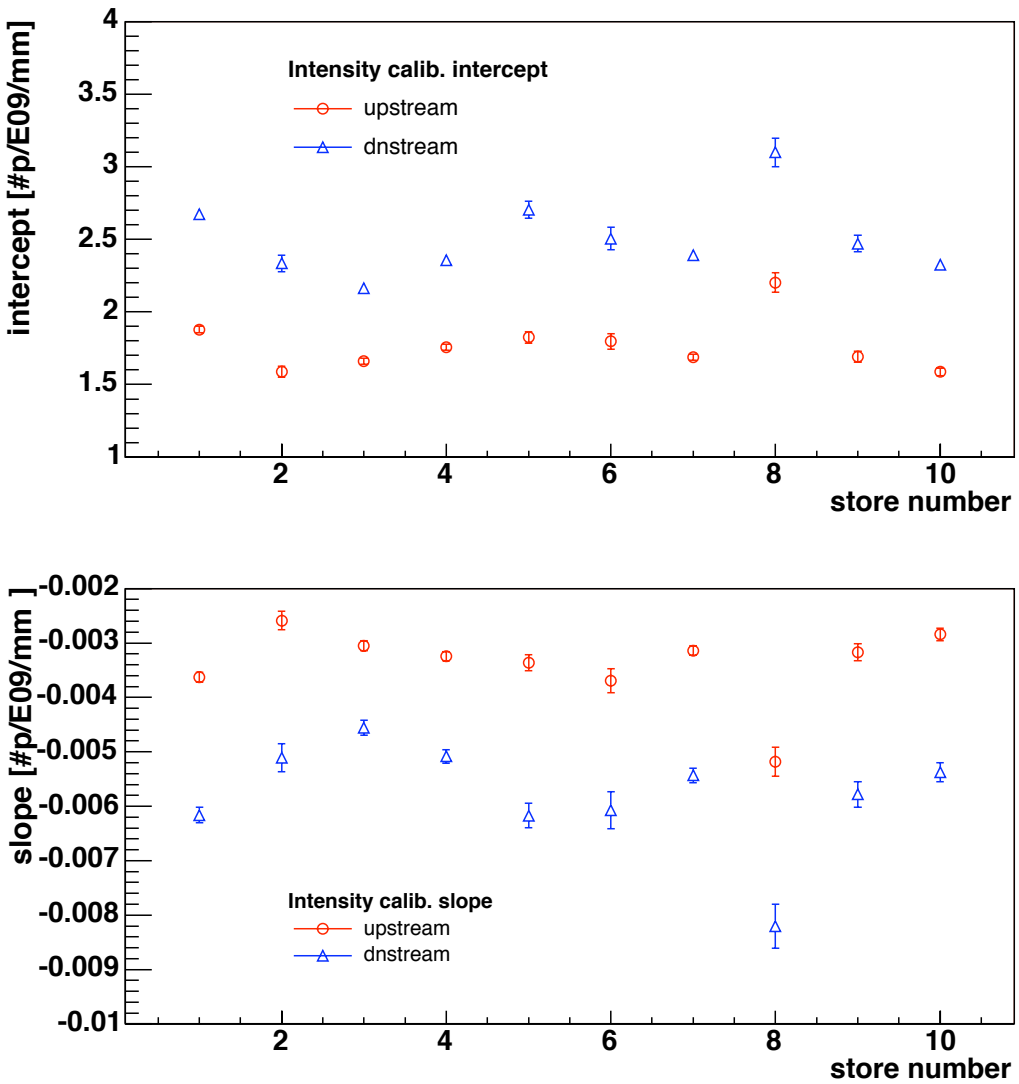

Figure 11: Slope (top) and intercept (bottom) for the correction function (equation 10) used in the horizontal acceptance ratio and intensity calibration for 10 stores. Stores 6200 and 6251 correspond to the horizontal axis values of 1 and 10, respectively.

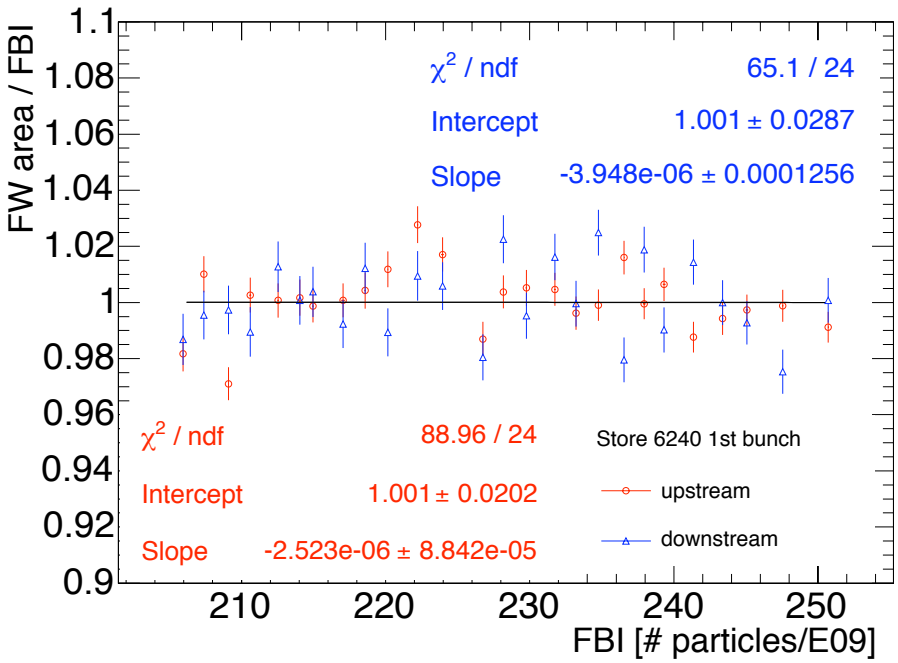

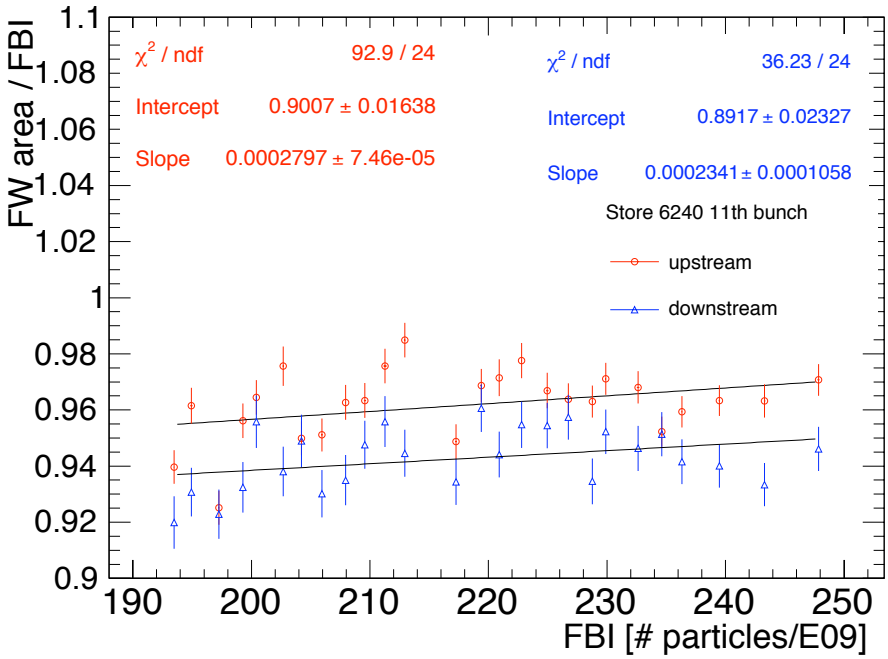

Figure 12: Ratio of FBI and horizontal FW intensity as a function of FBI for the 1st bunch (top) and the 11th bunch (bottom) in store 6240.

Table 5: Slope and intercept of the vertical correction function (equation 10) for the 10 stores.

	Upstream (pass1)		Downstream (pass0)	
Store	s	r_0	s	r_0
6200	-0.001790 ± 0.000090	1.219 ± 0.021	-0.003854 ± 0.000080	1.928 ± 0.019
6203	-0.001291 ± 0.000167	1.072 ± 0.037	-0.003065 ± 0.000152	1.694 ± 0.034
6214	-0.001311 ± 0.000086	1.059 ± 0.020	-0.002960 ± 0.000078	1.636 ± 0.018
6215	-0.001730 ± 0.000073	1.184 ± 0.018	-0.003545 ± 0.000067	1.818 ± 0.016
6216	-0.001639 ± 0.000144	1.178 ± 0.038	-0.003573 ± 0.000132	1.869 ± 0.034
6239	-0.001307 ± 0.000201	1.045 ± 0.047	-0.003891 ± 0.000179	1.837 ± 0.041
6240	-0.001420 ± 0.000079	1.081 ± 0.018	-0.003389 ± 0.000071	1.744 ± 0.016
6245	-0.002998 ± 0.000225	1.463 ± 0.055	-0.005453 ± 0.000204	2.260 ± 0.050
6250	-0.001569 ± 0.000151	1.110 ± 0.036	-0.003638 ± 0.000141	1.799 ± 0.033
6251	-0.001705 ± 0.000106	1.118 ± 0.024	-0.003427 ± 0.000098	1.711 ± 0.022

Before the calibration, the intensities measured by FW do not decrease as a function of time due to the intensity dependence of the detector response (top Figure 13). In addition, downstream profiles measure larger intensities than upstream profiles due to the difference in acceptance angles. After the calibration, both upstream and downstream FW profiles measure intensities close to those measured by the FBI, suggesting that the calibration removes these systematic effects (Figure 13 bottom).

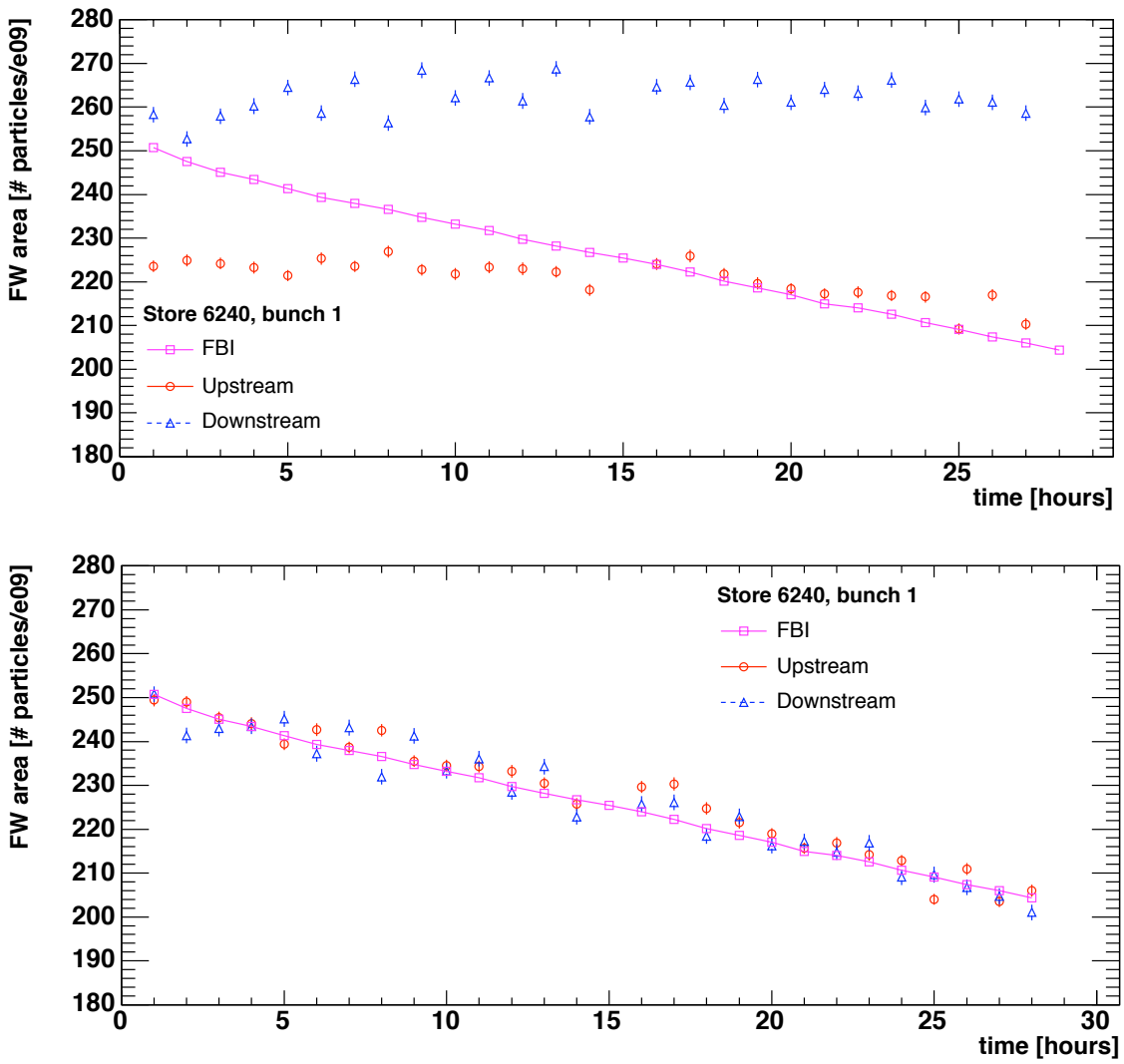

Figure 13: Beam intensity for the first bunch measured by horizontal FW for store 6240. Top is the beam intensity before acceptance and intensity calibration and bottom is the beam intensity after the calibration. The pink line is FBI.

3.5 Beam position

As noted in Section 2, the offline analysis program automatically adjusts the position of the upstream and downstream profiles so that their peaks overlay each other by introducing the "autorotation angle". However, the rotation values reported by the FW offline analysis program differ significantly for every fly. Therefore, we turned off the autorotation for stores 7106 and 7109 to investigate this effect. Horizontal peak positions of upstream and downstream profiles taken from the fits are shown in Figure 14. From the plots, we observe that upstream and downstream horizontal peaks are separated by 2.94 ± 0.02 mm for a CW fly and 4.24 ± 0.01 mm for a CCW fly. We only document this effect here. Differences in the autorotation do not affect our width analysis.

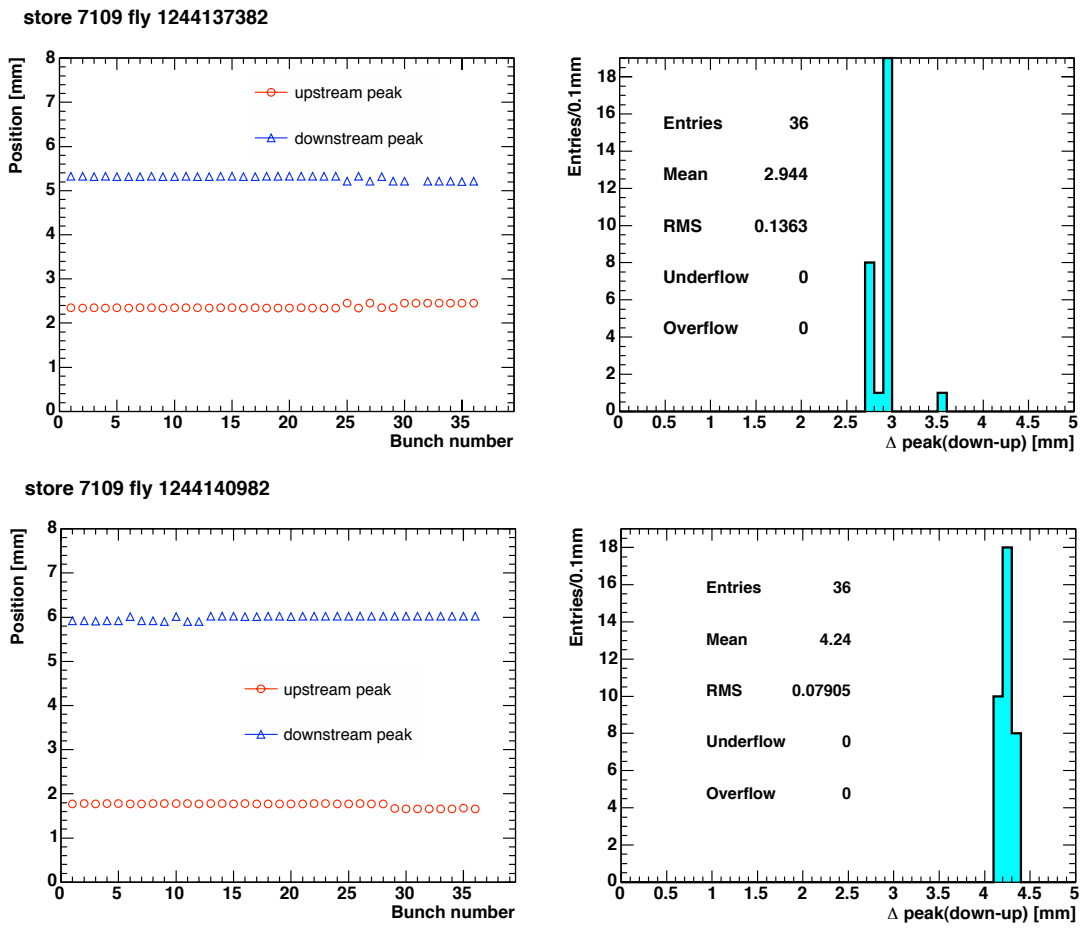

Figure 14: Peak positions and difference between upstream and downstream positions for 36 bunches in store 7106. Plots at the top are from a CW fly and plots at the bottom are from a CCW fly.

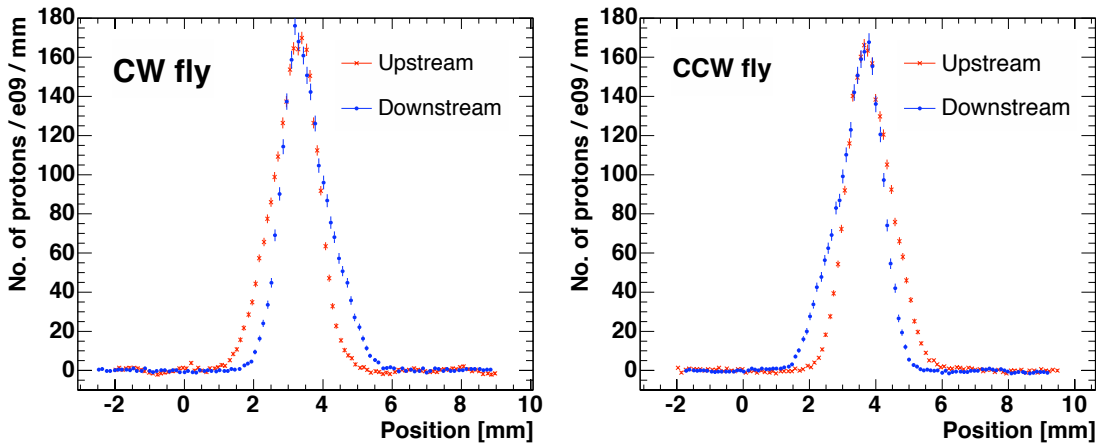

Figure 15: Horizontal FW data for a CW fly (left) and CCW fly (right) for the first bunch. The CW profiles are taken at 1213333060 and the CCW profiles are taken at 121336660 in store 6216. Upstream(red) and downstream(blue) profiles are translated and overlayed for comparison.

4 Data Analysis

4.1 Asymmetric Profiles and Scattering Model

Flying Wire beam profiles are asymmetric with the asymmetry depending on fly direction and interaction points (Figures 15 and 16). An upstream profile has a tail on the left and downstream profile has a tail on the right for a CW fly. The location of the tail is reversed for a CCW fly. This effect is observed in both horizontal and vertical data although the effect is more prominent in horizontal than vertical data. Since the location of the tail in the beam profile depends on the direction of wire movement, one possible explanation of the asymmetry is to interpret it as a result of scattering of beam by the wire. In our analysis, we use a scattering model to characterize the data.

The scattering model concept is shown in Figure 17. When the beam strikes the wire, particles are scattered. While a significant fraction of the particles are detected immediately, some particles will take longer to hit the detector or reach the limiting aperture. In this case, measurements taken later in the time will contain the direct scattering from beam at that wire position and other particles that were scattered from earlier wire positions (Figure 17). This process is mathematically described with a convolution of beam profile and distribution of scattered particles that are not absorbed immediately. We assume Gaussian PDFs for both beam and scattered particle

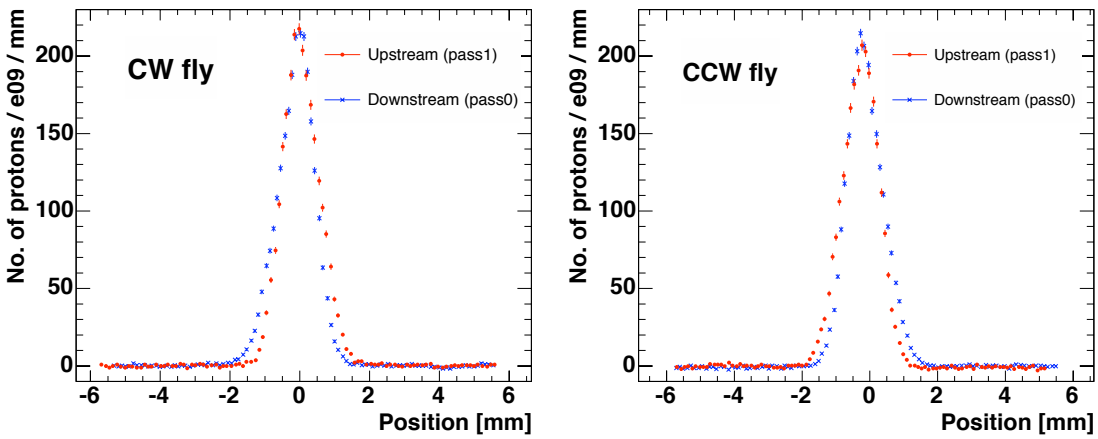

Figure 16: Vertical beam profiles measured by E11V FW for the same bunch as in Figure 15.

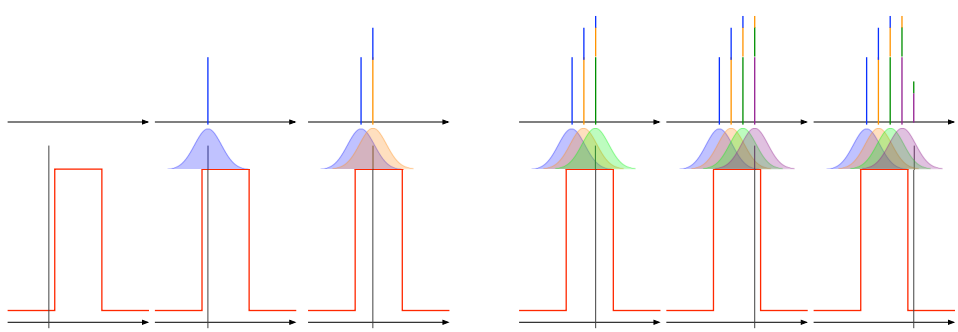

Figure 17: Conceptual illustration of scattering model. Red rectangular shape is the beam and curves are the scattered particles (blue, orange, green, and purple). The bar graph represents the beam loss detected by the FW system.

distributions. Equation (11) and (12) are the fit functions used in the analysis

$$h_R(x) = \frac{A}{\pi\sigma_B\sigma_S}\int_{-\infty}^{x} e^{-\frac{(x'-\mu)^2}{2\sigma_B^2}} e^{-\frac{(x-x')^2}{2\sigma_S^2}} \mathrm{d}x' \tag{11}$$

$$h_L(x) = \frac{A}{\pi\sigma_B\sigma_S}\int_{x}^{\infty} e^{-\frac{(x'-\mu)^2}{2\sigma_B^2}} e^{-\frac{(x-x')^2}{2\sigma_S^2}} \mathrm{d}x', \tag{12}$$

where σ_B is the width of Gaussian PDF for the beam and σ_S is the width of Gaussian PDF for the scattered particles. We integrate from $-\infty$ to position x if the wire is moving from smaller x to larger x (Eqn. 11), and integrate from x to $+\infty$ if the wire is moving from larger x to smaller x (Eqn. 12) as a function of time. The asymmetric integration limits account for events that have occurred only before the measurement. Figure 18 illustrates how this asymmetric convolution produces an asymmetric PDF from two Gaussian PDFs. Beam Gaussian PDF is represented as red graph, scattering PDF is represented as blue graph, and h_R and h_L are the pink and navy profiles. An interesting consequence of this asymmetric convolution is the peak position of h_R and h_L. The peaks of h_R and h_L are displaced from the peak of the beam Gaussian PDF and they depend on the integration range. Applying the scattering model to FW measurements, we predict a displacement of upstream and downstream beam profiles.

4.2 Fit to Data

In the fit to beam profiles, we add a linear function to h_R and h_L to accomodate for residual baseline shifts. As a result, we have 6 free parameters in the fit: 3 parameters from the beam Gaussian PDF (μ_B,σ_B, and A_B), one parameter from the scattering width (σ_S), and 2 parameters, slope and intercept, from the linear function. An example of the fit is shown in Figure 19 and 20 for horizontal and vertical profiles, respectively. Time dependence of the fit parameters is shown in Figure 21. As we expect, beam intensity (amplitude, A_B) decreases and beam width(σ_B) increases with time, and scattering width (σ_S) is roughly constant. The position of beam (μ_B) is bimodal, indicating the dependence on the direction of wire movement. Figure 22 overlay profiles taken at different times in the same store. We observe that the amplitude decreases and the width increases with time for both upstream and downstream profiles.

4.3 Extracting the Diffusion Rate

Using the scattering model, we characterize the beam profiles with a Gaussian PDF describing the beam and the width of the scattering distribution, σ_S. Although σ_S is a free parameter in the fit, horizontal fit results indicate σ_S is roughly constant ($\sim 1.2\%$ variation) for all bunches for the 10 stores. Average of σ_S from horizontal fits through the store are shown in Figure 23 for all 36 bunches.

This consistency is representative of all 10 stores for horizontal profiles. Therefore, we take $d\sigma_B/dt$ as the horizontal beam width growth rate. An example of the beam

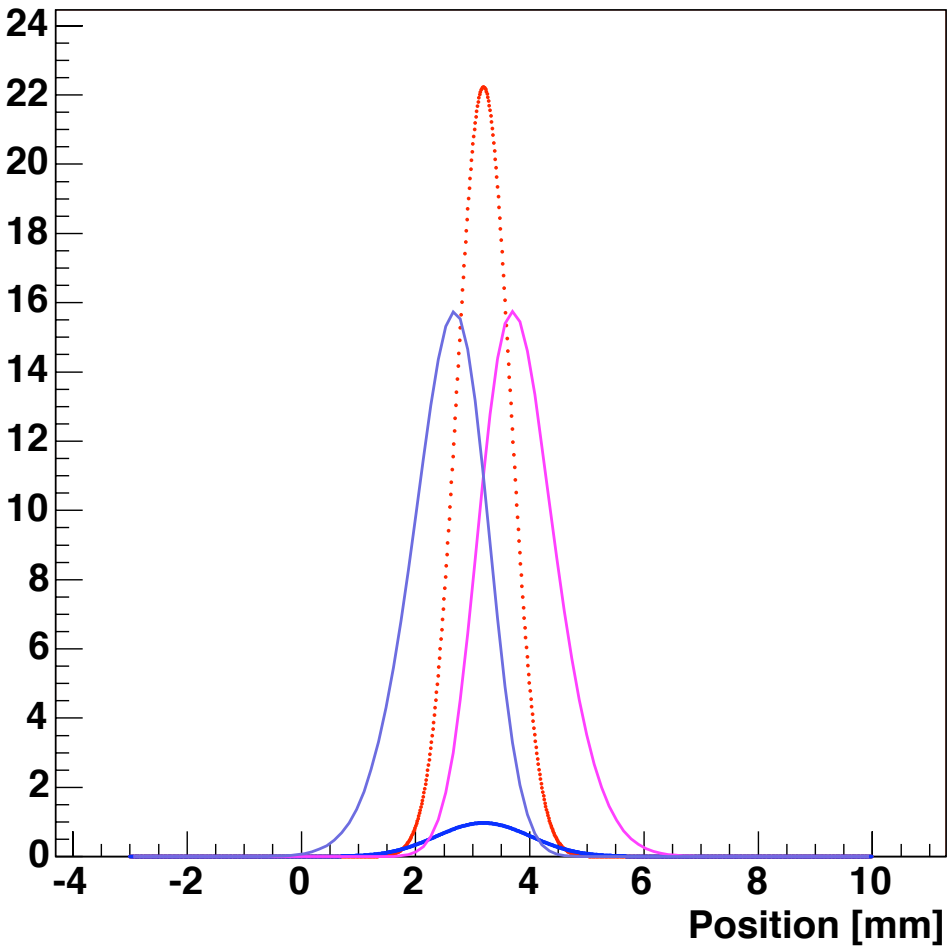

Figure 18: Illustration of how the asymmetric profiles are made from asymmetric convolution. Red Gaussian PDF is the beam Gaussian PDF, blue Gaussian PDF is the scattering distribution, and pink is h_R and navy is h_L.

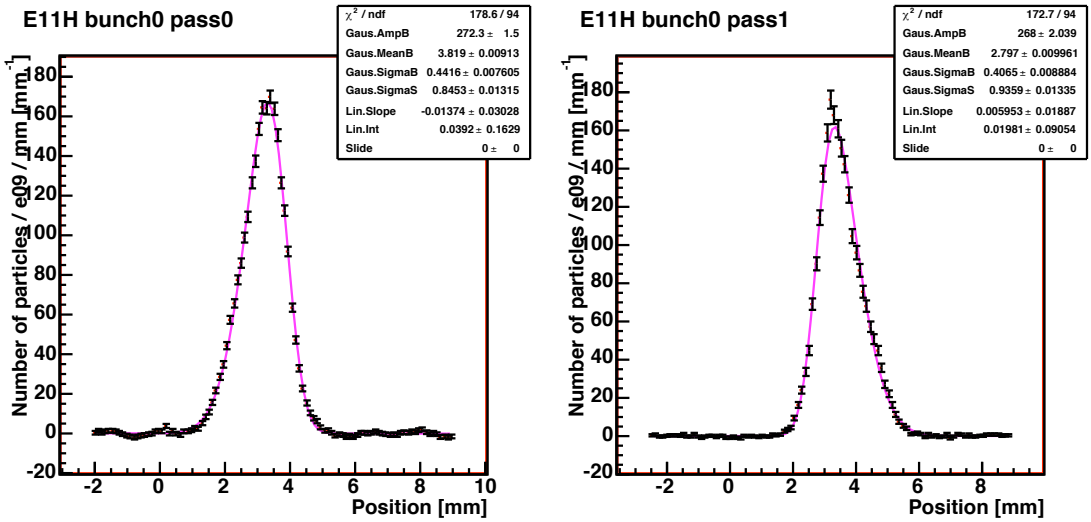

Figure 19: Fit to horizontal beam profile using scattering model. Store 6216 fly 1213333060.

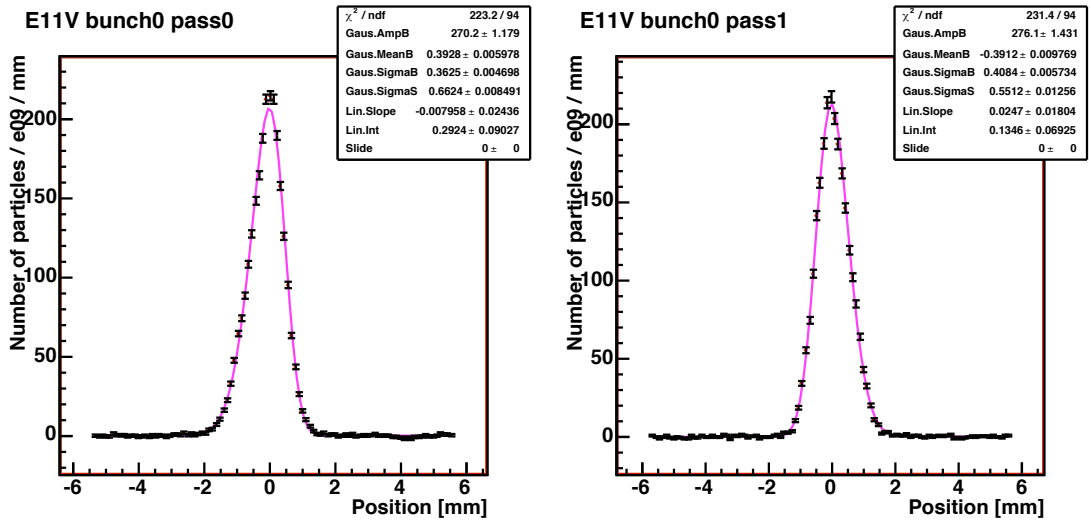

Figure 20: Fit to vertical beam profiles using scattering model. Store 6216 fly 1213333060.

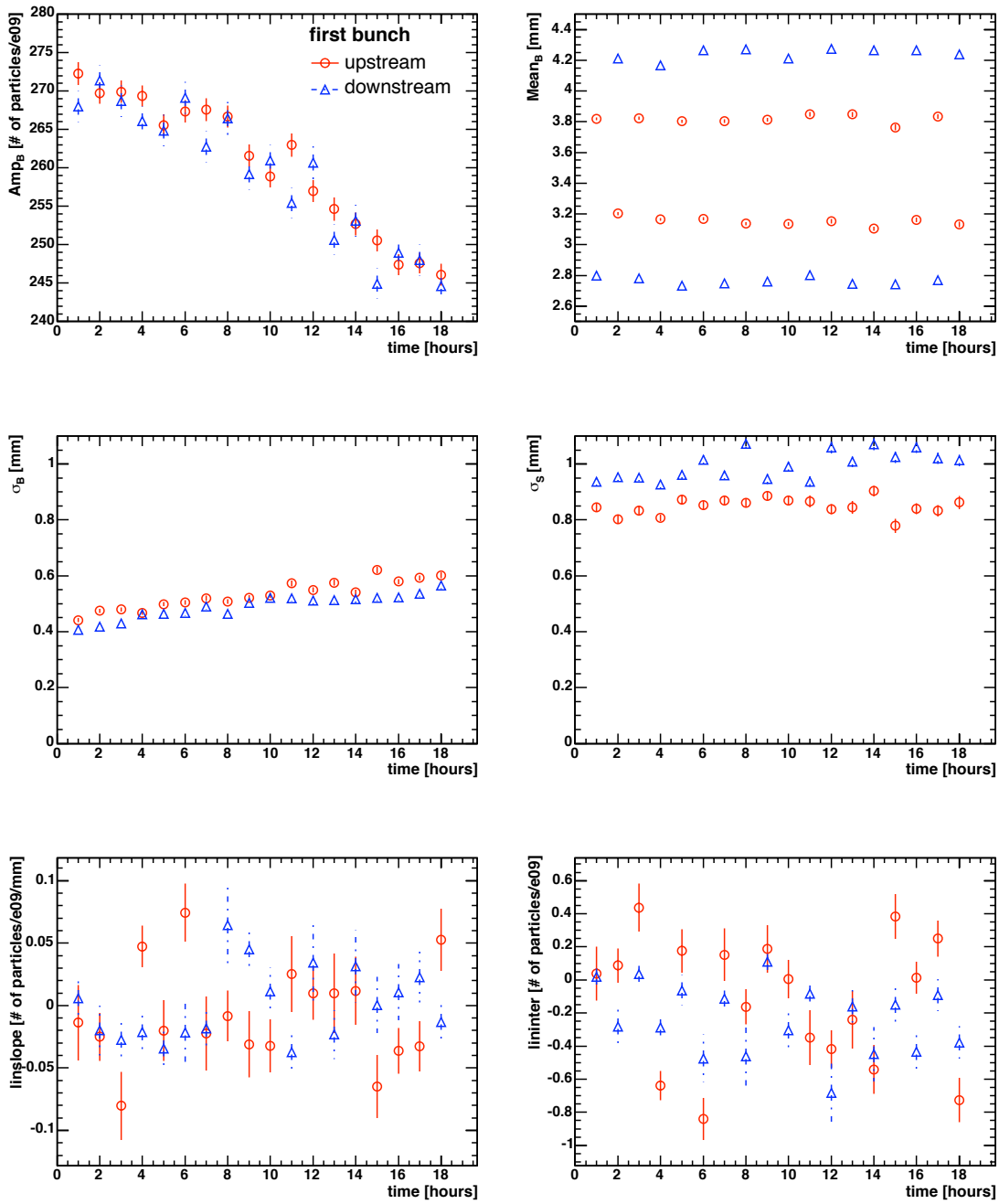

Figure 21: Horizontal fit parameters for the first bunch as a function of time for store 6216. Red circles are for upstream and blue triangles are for downstream profiles.

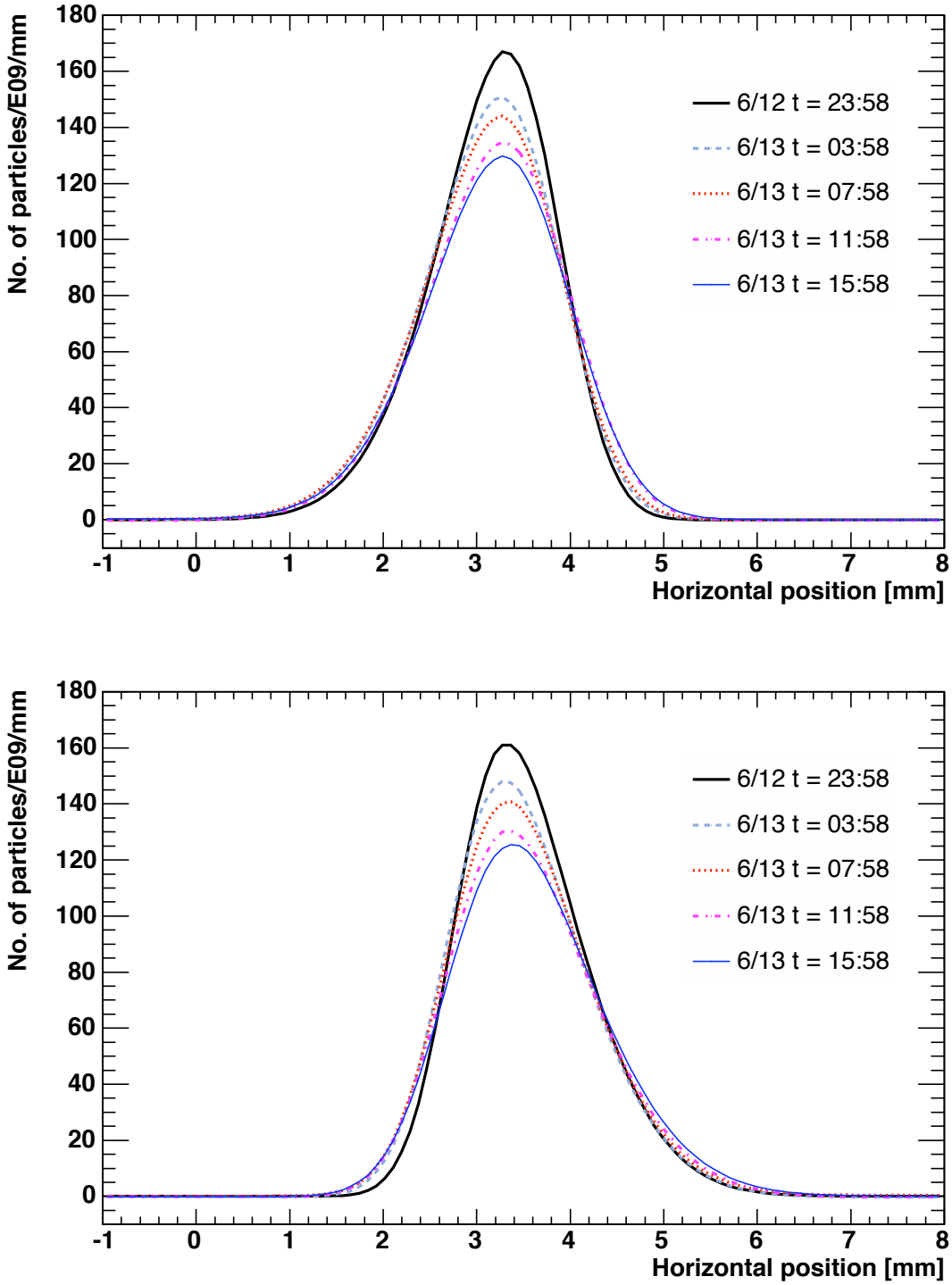

Figure 22: Horizontal profiles change as a function of time. First bunch in store 6216.

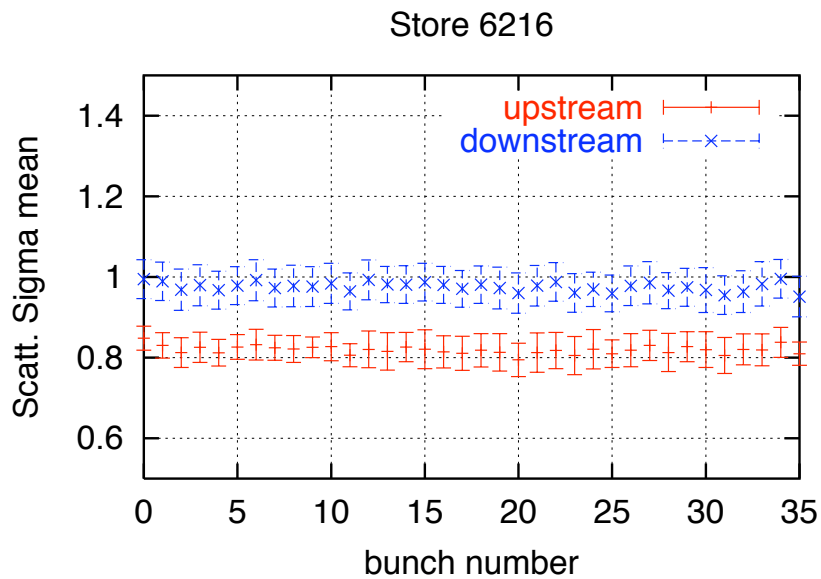

Figure 23: Horizontal σ_S for each bunch for the 10 stores. Each point is the average of σ_S of the particular bunch for the entire store.

width as a function of time in the store is shown in Figure 24. Beam width growth rate is extracted by fitting a linear function. The horizontal $d\sigma_B/dt$ and its uncertainty for the 10 stores are shown in Table 6 and plotted in Figure 25. The average horizontal beam width growth rate, for upstream and downstream, is $(8.89\pm0.02)\times10^{-3}$mm/hour. Change in horizontal σ_B^2 is listed in Table 7 and plotted in Figure 26. The average $d\sigma_B^2/dt$ is $(8.93\pm0.01)\times10^{-3}$ mm^2/hour. Vertical diffusion rate is also measured using the same technique. However, vertical profiles are more symmetric than horizontal profiles, and as a consequence, σ_B and σ_S are $\sim 80-90\%$ correlated in the fit. This correlation makes fits difficult, and fits seem to converge to two possible local minima. Tables 8 and 9 show results of the vertical beam width growth rate for the stores whose fit returns similar values of σ_S as horizontal profiles. The average vertical $d\sigma_B/dt$ is $(7.04\pm0.01)\times10^{-3}$mm/hour and $d\sigma_B^2/dt$ is $(6.24\pm0.01)\times10^{-3}$ mm^2/hour.

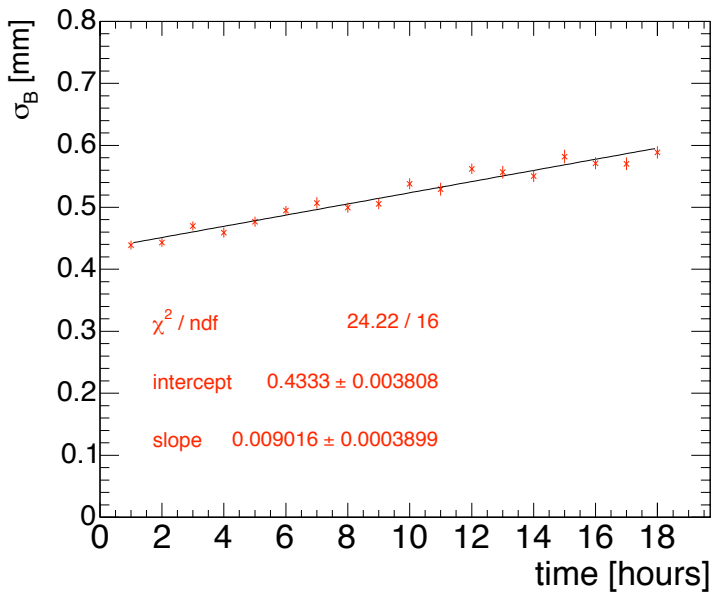

Figure 24: Store 6216, upstream first bunch width as a function of time in store.

4.4 Comparison of Beam Width with Synclite

As a crosscheck, we compare our measurement of beam width with Synclite. Horizontal beam emittance is calculated using the beam width from both FW and synclite. We calculate 95% normalized emittance using

$$\epsilon_N = \frac{6\pi(\beta_L\gamma_L)}{\beta_{lattice}}(\sigma^2 - D^2(\frac{dp}{p})^2), \tag{13}$$

where σ is beam width, D is dispersion, and $\frac{dp}{p}$ is the fractional momentum spread taken from ACNET variable, T:SBDPMS. Lattice functions used for the calculation are listed in Table 10. Synclite beam width is taken from ACNET variables, T:SLPSH and T:SLPSV. The calculated emittance for a bunch in store 6216 is shown in Figure 27. The emittance calculated from Synclite is larger than those calculated from FW for both horizontal and vertical measurements. Causes for the difference are not fully understood. One possible uncertainty in the FW measurement is that the free parameter, σ_S, may not be chosen correctly. Since σ_B and σ_S are correlated in the fit, choosing a σ_S that is too large can cause our measurement of σ_B to be too small. Further analysis is necessary to understand this effect. Lattice measurements, which may have fairly large uncertainties, may be another possible source of the discrepancy.

5 Conclusions

Horizontal and vertical proton profiles measured by the FW in the Tevatron have been analyzed. We observe mechanical effects such as a difference in acceptance ratio

Table 6: Horizontal beam width growth rate, $d\sigma_B/dt$ for the 10 stores.

Store	$d\sigma_B/dt_{UP}$ [mm/hr]	$d\sigma_B/dt_{DN}$ [mm/hr]
6200	0.009236 ± 0.000048	0.009749 ± 0.000052
6203	0.010476 ± 0.000110	0.010906 ± 0.000117
6214	0.008352 ± 0.000041	0.008182 ± 0.000046
6215	0.007483 ± 0.000031	0.007761 ± 0.000035
6216	0.008392 ± 0.000065	0.008010 ± 0.000068
6239	0.009365 ± 0.000089	0.009685 ± 0.000095
6240	0.006994 ± 0.000037	0.007421 ± 0.000040
6245	0.009651 ± 0.000080	0.010546 ± 0.000087
6250	0.009631 ± 0.000075	0.009127 ± 0.000081
6251	0.008680 ± 0.000055	0.008225 ± 0.000061

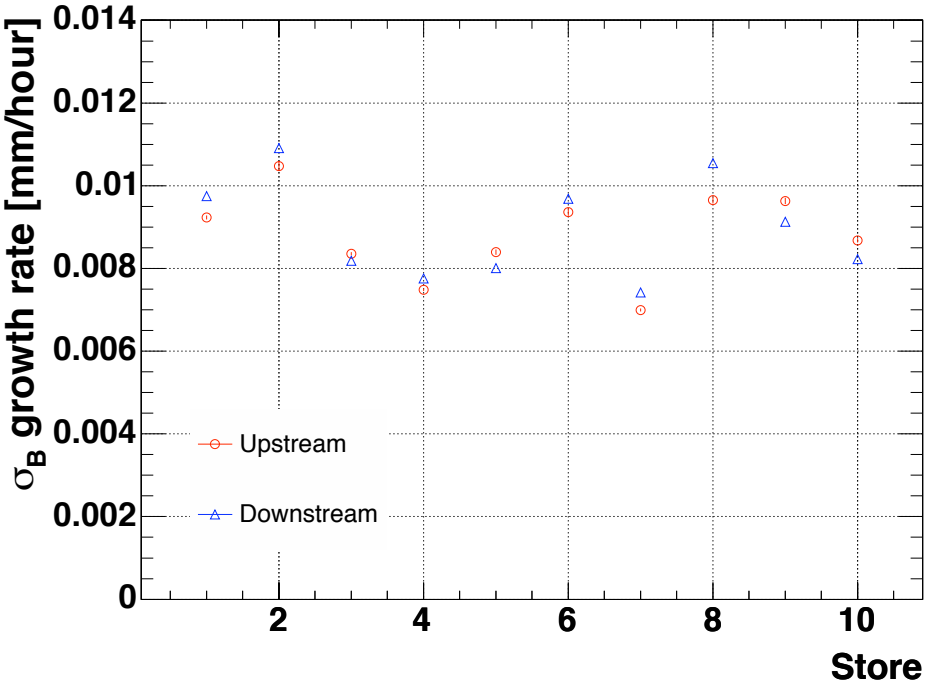

Figure 25: Beam width growth rate for the 10 stores.

Table 7: Horizontal diffusion rate, $d\sigma_B^2/dt$, for the 10 stores.

Store	$d\sigma_B^2/dt_{UP}$ [mm^2/hr]	$d\sigma_B^2/dt_{DN}$[mm^2/hr]
6200	0.010184 ± 0.000037	0.010035 ± 0.000039
6203	0.010499 ± 0.000078	0.010332 ± 0.000080
6214	0.008932 ± 0.000031	0.007944 ± 0.000033
6215	0.008073 ± 0.000023	0.007663 ± 0.000025
6216	0.008727 ± 0.000048	0.007646 ± 0.000048
6239	0.009676 ± 0.000065	0.009115 ± 0.000067
6240	0.007781 ± 0.000029	0.007684 ± 0.000031
6245	0.010201 ± 0.000057	0.009072 ± 0.000059
6250	0.009737 ± 0.000054	0.008553 ± 0.000056
6251	0.008931 ± 0.000041	0.007867 ± 0.000043

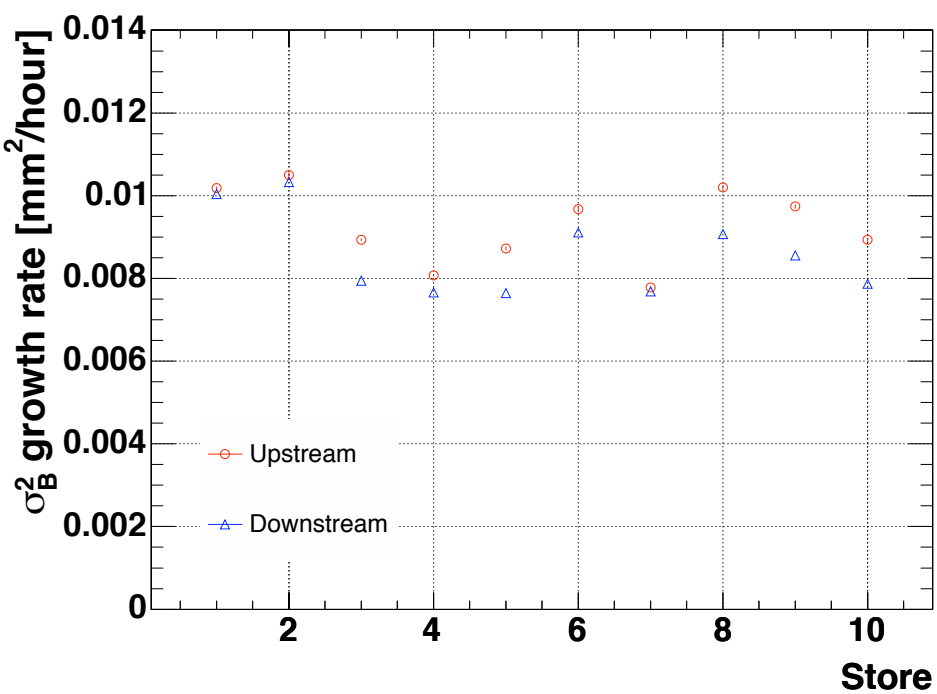

Figure 26: Horizontal diffusion rate, $d\sigma_B^2/dt$, for the 10 stores.

Table 8: Vertical beam width growth rate, $d\sigma_B/dt$ for 6 selected stores.

Store	$d\sigma_B/dt_{UP}$ [mm/hr]	$d\sigma_B/dt_{DN}$ [mm/hr]
6200	0.008389 ± 0.000034	0.007113 ± 0.000031
6214	0.007803 ± 0.000031	0.007127 ± 0.000027
6216	0.006100 ± 0.000046	0.005970 ± 0.000040
6240	0.005705 ± 0.000032	0.006028 ± 0.000028
6250	0.008138 ± 0.000052	0.008170 ± 0.000046
6251	0.006849 ± 0.000042	0.007040 ± 0.000037

Table 9: Vertical diffusion rate, $d\sigma_B^2/dt$ for 6 selected stores.

Store	$d\sigma_B^2/dt_{UP}$ [mm^2/hr]	$d\sigma_B^2/dt_{DN}$[mm^2/hr]
6200	0.008209 ± 0.000021	0.006182 ± 0.000019
6214	0.007357 ± 0.000020	0.005984 ± 0.000016
6216	0.005605 ± 0.000028	0.004784 ± 0.000023
6240	0.005633 ± 0.000021	0.005454 ± 0.000018
6250	0.007167 ± 0.000031	0.006603 ± 0.000026
6251	0.006098 ± 0.000026	0.005777 ± 0.000021

Table 10: Beta functions and dispersion at Synclite and E11 FWs. Dispersion in vertical plane is taken as 0. These values are taken from Lattice Database [7].

	$\beta_{xlattice}$[m]	D_x [m]	$\beta_{ylattice}$[m]
Synclite	52.37	1.65	110.38
FW E11H	90.00	1.99	–
FW E11V	–	–	81.07

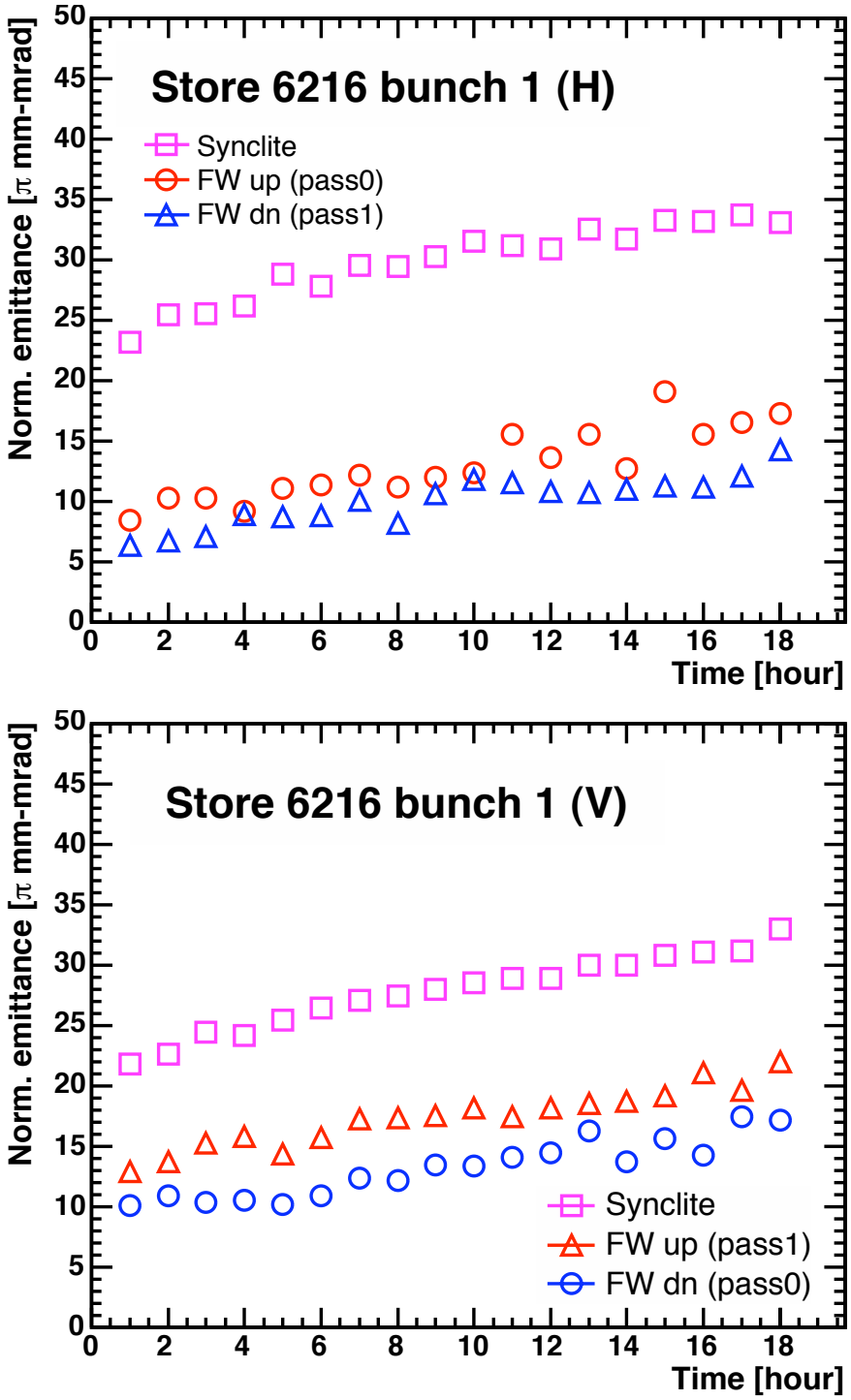

Figure 27: Normalized 95% horizontal (left) and vertical (right) emittance calculated form Synclite and FW measurement for store 6216.

Table 11: Horizontal and vertical beam width growth rate ($d\sigma_B/dt$) and diffusion rate ($d\sigma_B^2/dt$).

	$d\sigma_B/dt$ [mm/hr.]	$d\sigma_B^2/dt$ [mm^2/hr.]	$d\epsilon_N/dt$ [π mm-mrad/hr.]
Horizontal	$(8.89 \pm 0.02) \times 10^{-3}$	$(8.93 \pm 0.01) \times 10^{-3}$	–
Vertical	$(7.04 \pm 0.01) \times 10^{-3}$	$(6.24 \pm 0.01) \times 10^{-3}$	~ 0.48

between upstream and downstream profiles, intensity dependent detector response, and asymmetric beam profiles. The first two effects have been calibrated against FBI measurements. We have proposed a scattering model that could explain the asymmetric profiles. Measurement of horizontal and vertical beam growth rate for the proton beam in the Tevatron during typical stores is listed in Table 11. A way to improve the measurement is to investigate the difference between FW and Synclite emittance measurement.

Acknowledgements

We are grateful for Young-Kee Kim, Mike Syphers, Jim Zagel, and Dave Slimmer for their support and useful discussions.

References

[1] M. J. Syphers, "An Analytical Approach to Understanding Tevatron Integrated Luminosity", Fermilab-FN-08020-AD, May 2007.

[2] J. Zagel, M. Hu, A. Jansson, R. Thurman-Keup, and M. J. Yang, "Complementary Method of Transverse Emittance Measurement", BIW08, Lake Tahoe, CA, May 2008.

[3] J. Utterback, G. Vogel, "Fast Bunch Integrator: A system for measuring bunch intensities in Fermilab main ring", ICALEPCS 95, Chicago, IL, Oct. 1995.

[4] G. Vogel, "Tevatron Flying Wire system description", www-inst.fnal.gov/global/TFW/SystemDoc/TFWDescr.html, 1997.

[5] C. Christensen, "Flying Wire Geometry", Beams-doc-765-v5, 2003.

[6] E. Lorman, "Flying Wire Analysis," Octorber 2003.

[7] Fermilab Lattice Functions. Tevatron (storephysics), http://www-bd.fnal.gov/lattices/seeLattice.php?id=82&machine=Tevatron&client=storephysics.

[8] V. Shiltsev, A. Tollesrup, "Study of IBS in Tevatron," Beams-Doc-1519-v2.

[9] L. Y. Nicolas, "Radiation Environment Simulation at the Tevatron, Studies of the Beam Profile, and Measurement of B_c Meson Mass", University of Glasgow, 2005.

[10] E.N. Tsyganov, *FermilabPreprint* TM-682, TM-684, 1976.

[11] A.A. Elishev, *Phys.Lett.* B**88**, 387, 1979.

[12] M. Church, "Tevatron Run-II Beam Collimation System", FERMILAB-Conf-99/059, 1999.